

Topological Phases in Fractals: Local Spin Chern Marker in the Sierpinski carpet Kane-Mele-Rashba Model

L. L. Lage,^{1,*} A. B. Félix,¹ S. dos A. Sousa-Júnior,² A. Latgé,¹ and Tarik P. Cysne^{1,†}

¹*Instituto de Física, Universidade Federal Fluminense,
Niterói, Av. Litorânea sn 24210-340, RJ-Brazil*

²*Department of Physics, University of Houston, Houston, Texas 77004, USA*
(Dated: March 5, 2025)

We study the spectral properties and local topology of the Kane-Mele-Rashba model on a Sierpinski Carpet (SC) fractal, constructed from a rectangular flake with an underlying honeycomb arrangement and open boundary conditions. When the system parameters correspond to a topologically trivial phase, the energy spectrum is characterized solely by bulk states that are not significantly modified by the system's fractality. For parameters corresponding to the quantum spin Hall insulator (QSHI) phase, in addition to bulk states, the energy spectrum exhibits in-gap topological states that are strongly influenced by the fractal geometry. As the fractal generation increases, the in-gap topological states acquire a staircase profile, which translates into sharp peaks in the density of states. We also show that both the QSHI and the trivial phase exhibit a large gap in the valence-projected spin spectrum, allowing the use of the local spin Chern marker (LSCM) to index the local topology of the system. Fractality does not affect this gap, allowing the application of LSCM to higher fractal generations. Our results explore the LSCM versatility, showing its potential to access local topology in complex geometries such as fractal systems.

I. INTRODUCTION

Fractal geometries, characterized by self-similarity and non-integer dimensionality, have emerged as a rich playground for exploring the interplay between geometry, topology, and quantum mechanics. Among these, the structure of a Sierpinski fractal, recursively constructed with a hierarchical geometry, has garnered significant attention due to its unique spectral properties and potential applications in condensed matter physics with recent experimental realizations [1–3] and theoretical investigations [4–10]. In particular, the Sierpinski carpet (SC) is a self-similar fractal system with a Hausdorff dimension of $\log_3(8) \approx 1.8928$. It is constructed through an iterative process of subdividing a solid square into a 3×3 grid of smaller congruent squares and removing the central square. This process is repeated recursively for each of the remaining eight squares, resulting in a structure composed of self-replicated solid squares, as shown in Fig. 1. Studies have explored the consequences of fractality in charge and spin transport and the Hofstadter spectrum of electrons in SC fractal geometry [8, 11–14].

In recent years, the field of topological phases of matter has witnessed remarkable progress, driven by the discovery of topological insulators and superconductors. In the band-theory perspective [systems in the thermodynamic limit with translation symmetry] the topological phases are characterized by bulk topological invariants that index the global properties of a system [15]. These invariants are protected by a gapped bulk

energy spectrum and remain unchanged under smooth variations in the electronic Hamiltonian. Non-trivial topology presents physically measurable consequences. For example, the Chern insulators proposed by Haldane [16] are indexed by a topological invariant called the Chern number and are characterized by a quantized Hall conductivity. This conductivity is enabled by the emergence of edge states when the system is prepared, for instance, in a nanoribbon geometry. Similarly, the quantum spin Hall insulators (QSHI) introduced by Kane and Mele [17, 18] are characterized by a finite spin-Hall conductivity within the insulating bulk energy gap. This conductivity is enabled by spin-polarized edge states that appear in a nanoribbon geometry. QSHIs can be indexed by a \mathbb{Z}_2 invariant protected by time-reversal symmetry. However, in systems with broken translational invariance, such as fractals, quasicrystals, or disordered lattices the global topological indexation may lose its meaning, requiring a local description of topological properties. Added to this, from a fundamental point of view, studying topological aspects of fractals is appealing because their non-integer Hausdorff dimension does not fit into the ten-fold way topological classification [19, 20].

Local markers have emerged as a powerful tool for addressing the challenge of topological indexing systems that lack translational symmetry. By providing a real-space measure of topological invariants, local markers enable the characterization of topological phases in systems with complex geometries or a high degree of disorder [21–24]. It has also been used to study strongly correlated topological systems in different models [25–27]. This approach is particularly relevant for Sierpinski fractals in which the interplay between fractal geometry and topology can lead to novel phenomena, such as hierarchical edge states [6], self-similar energy spectra

* lucaslage@id.uff.br

† tarik.cysne@gmail.com

[28–30], and fractality-induced topological phases [31].

Experimental setups in bismuth fractal flakes were recently investigated and highlighted the importance of including Rashba spin-orbit coupling (RSOC) effects in describing such systems [32]. The RSOC is associated with the breaking of ($z \rightarrow -z$)-symmetry produced by the proximity of materials to a substrate and causes the electronic Hamiltonian to break spin conservation, $[\mathcal{H}, \hat{s}_z] \neq 0$. A local marker description of the QSHI phase for systems with strong RSOC was recently developed [33]. The local spin Chern marker (LSCM) combines the local Chern number introduced by Bianco and Resta [34] with Prodan’s spin Chern number approach, which was constructed in Ref. [35] assuming the thermodynamic limit. The LSCM was applied to describe the local topology of generalized classes of Kane-Mele-Rashba models [36], demonstrating its versatility as a tool for real-space topological indexation.

Motivated by the previous discussion, we investigate the local topology of the Kane-Mele-Rashba model in the SC geometry using the LSCM. Studies of SC geometry in an underlying honeycomb mesh have been motivated by potential applications in graphene-based fractal nanostructures [12, 37–40]. In principle, Kane-Mele-Rashba model could be realized in graphene through the proximity effect to a suitable substrate [41–47]. Given the maturity of nanofabrication technology for two-dimensional materials, graphene can play an important role in the experimental understanding of the topological nature of quantum fractals. Other systems in which the Kane-Mele-Rashba model shares similarities include graphene family materials [48–50] and bismuthene grown in SiC [51, 52].

II. MODEL AND METHODS

A. Kane-Mele-Rashba Hamiltonian in Sierpinski Carpet

The Kane-Mele-Rashba Hamiltonian can be cast as,

$$\begin{aligned} \mathcal{H}_{\text{KMR}} = & t \sum_{s=\uparrow,\downarrow} \sum_{\langle \mathbf{i}, \mathbf{j} \rangle} c_{\mathbf{i},s}^\dagger c_{\mathbf{j},s} + V_{\text{ab}} \sum_{s=\uparrow,\downarrow} \sum_{\mathbf{i}} \tau_{\mathbf{i}} c_{\mathbf{i},s}^\dagger c_{\mathbf{i},s} \\ & + i\lambda_{\text{KM}} \sum_{s,s'} \sum_{\langle \langle \mathbf{i}, \mathbf{j} \rangle \rangle} \nu_{\mathbf{ij}} c_{\mathbf{i},s}^\dagger (\hat{s}_z)_{s,s'} c_{\mathbf{j},s'} \\ & + i\lambda_{\text{R}} \sum_{s,s'} \sum_{\langle \mathbf{i}, \mathbf{j} \rangle} c_{\mathbf{i},s}^\dagger [(\hat{\mathbf{s}} \times \mathbf{d}_{\mathbf{ij}})_z]_{s,s'} c_{\mathbf{j},s'}, \quad (1) \end{aligned}$$

where the first term represents the nearest neighbor hopping of electrons, with $c_{\mathbf{i},s}^\dagger$ and $c_{\mathbf{j},s}$ being the fermionic creation and annihilation operators for electrons at sites \mathbf{i} and \mathbf{j} of the lattice and spin $s = \uparrow, \downarrow$; $\langle \mathbf{i}, \mathbf{j} \rangle$ indicate a sum running over nearest neighbor sites. In all results presented in this work, we set the hopping amplitude t as the unit of energy [$t = -1$]. The second term is the sublattice potential. $\tau_{\mathbf{i}} = +1$ for sites \mathbf{i} belonging to

sublattice A of honeycomb structure, and $\tau_{\mathbf{i}} = -1$ for sites \mathbf{i} belonging to sublattice B of honeycomb structure. The third term is the Kane-Mele spin-orbit coupling that gives rise to the QSHI phase. $\nu_{\mathbf{ij}} = \text{sign}(\mathbf{d}_1 \times \mathbf{d}_2)_z = \pm 1$, where \mathbf{d}_1 and \mathbf{d}_2 are unit vectors along the two bonds that the electron crosses when jumping from the site \mathbf{j} to the next nearest neighbor \mathbf{i} [indicated in Eq.(1) by $\langle \langle \mathbf{i}, \mathbf{j} \rangle \rangle$]. Finally, the fourth term is the Rashba spin-orbit coupling \mathcal{H}_{R} . $\mathbf{d}_{\mathbf{ij}}$ is the unity vector along the direction connecting site \mathbf{i} to site \mathbf{j} , $\hat{\mathbf{s}} = \hat{s}_x \mathbf{x} + \hat{s}_y \mathbf{y} + \hat{s}_z \mathbf{z}$ is related to physical spin of electrons (up to a factor $\hbar/2$), and $\hat{s}_{x,y,z}$ are Pauli matrices. The Rashba coupling breaks ($z \rightarrow -z$)-symmetry [53] and is responsible for the non-conservation of spin in the full Hamiltonian $[\mathcal{H}_{\text{R}}, \hat{s}_z] \neq 0$.

The model described by Eq.(1) is applied to the lattices shown in Fig. 1, illustrating different generations of SC. A rectangular flake corresponds to a zero-order SC and it is shown in Fig.1(a) [G(0)]. Figs. 1(b)-(d) show the first [G(1)], second [G(2)], and third [G(3)] SC generations, respectively. Open boundary conditions (OBC) are used in the numerical calculation. We call attention to an important aspect of the construction presented in Fig. 1: When SC is built on an underlying square lattice, it has a four-fold rotation symmetry [C_4]. However, the used SC is based on a honeycomb lattice, and the entire structure exhibits two-fold rotation symmetry [C_2]. In fact, it is clear from Fig. 1 that while the upper and lower boundaries terminate in zigzag edges, the left and right boundaries are armchair edges. As shown in Ref. [12], the SC in the underlying honeycomb lattice exhibits typical fractal features and the expected Hausdorff dimension is $d_{\text{H}} \approx 1.89$.

B. Local Spin Chern Marker

We employ the LSCM [33, 36, 54, 55] to study the local topology of Hamiltonian from Eq.(1) in SC lattices. The LSCM is defined by

$$\mathfrak{C}_s(\mathbf{r}) = \frac{\mathfrak{C}_+(\mathbf{r}) - \mathfrak{C}_-(\mathbf{r})}{2}, \quad (2)$$

where,

$$\mathfrak{C}_\sigma(\mathbf{r}) = 2\pi \text{Im} \langle \mathbf{r} | \mathcal{Q}_\sigma \hat{X} \mathcal{P}_\sigma \hat{Y} \mathcal{Q}_\sigma - \mathcal{P}_\sigma \hat{X} \mathcal{Q}_\sigma \hat{Y} \mathcal{P}_\sigma | \mathbf{r} \rangle, \quad (3)$$

with \hat{X} and \hat{Y} being the components of the position operators $\hat{\mathbf{r}}$. To construct \mathcal{Q}_σ and \mathcal{P}_σ , one first needs to build the valence state projectors $\mathcal{P} = \sum_{n=1}^{N_{\text{occ}}} |u_n\rangle \langle u_n|$, where $|u_n\rangle$ is the eigenstate of the SC lattice model Hamiltonian \mathcal{H}_{KMR} with state index $n = (1, \dots, 2N)$, N is the number of sites while N_{occ} is the number of occupied states. Here, N_{occ} corresponds to a half filling, unless explicitly stated otherwise. Then, we construct the spin matrix projected onto the valence subspace $M_{\text{v.s.}}^{s_z} = \mathcal{P} \hat{s}_z \mathcal{P}$ and perform its diagonalization $M_{\text{v.s.}}^{s_z} |\phi_v\rangle = \xi_v^{s_z} |\phi_v\rangle$, where ($v = 1, \dots, N_{\text{occ}}$). For time-reversal symmetric models, the N_{occ} eigenvalues

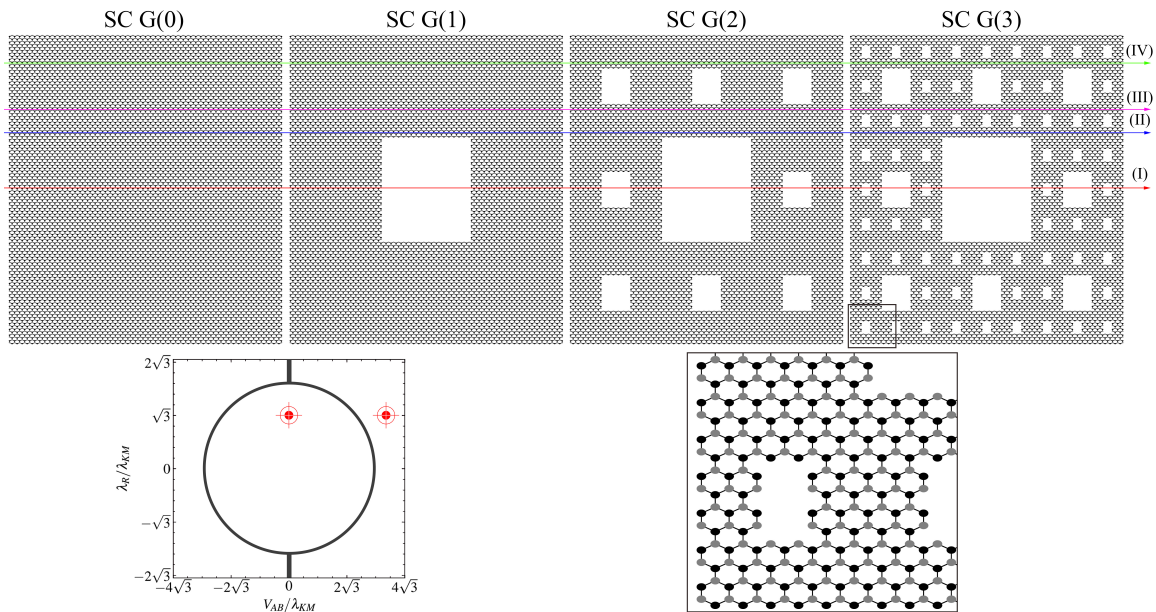


FIG. 1. Upper row: Sierpinski Carpets (SCs) with a honeycomb mesh for the first three fractal orders. Colored arrows (I)–(IV) indicate paths for LSCM calculations in Fig. 5. The number of sites in each generation is $N = 11988$ [G(0)], $N = 10512$ [G(1)], $N = 9456$ [G(2)], and $N = 8688$ [G(3)]. Bottom row: (left) Schematic of the topological phase diagram for the Kane-Mele-Rashba model, with red targets marking parameter sets for QSHI and trivial phases. (right) Magnified view of the honeycomb mesh used in the fractal construction.

$\xi_v^{s_z}$ are symmetrically distributed around zero within the interval $[-1, 1]$. The branches of this spectrum can be separated by the sign of their eigenvalues [$\sigma = +/ -$ for positive/negative $\xi_v^{s_z}$, respectively], if there is a finite gap Δ^{s_z} . The normalized eigenvectors of $M_{v.s.}^{s_z}$, $|\phi_v\rangle$, has dimension N_{occ} and can be written as $|\phi_v\rangle = (\beta_{1,v}, \beta_{2,v}, \dots, \beta_{N_{\text{occ}},v})^T$, T meaning the transpose operation. We then define the states,

$$|\psi_v\rangle = \sum_{\alpha=1}^{N_{\text{occ}}} \beta_{v,\alpha} |u_\alpha\rangle, \quad (4)$$

in terms of the valence eigenstates $|u_\alpha\rangle$ of the SC lattice model Hamiltonian \mathcal{H}_{KMR} . The projectors used in Eq. (3) are given by

$$\mathcal{P}_\sigma = \sum_{\xi_v^{s_z} | \text{sign}[\xi_v^{s_z}] = \sigma} |\psi_v\rangle \langle \psi_v|. \quad (5)$$

Finally, the complementary matrices in Eq. (3) are defined as $\mathcal{Q}_\sigma = \mathbb{1} - \mathcal{P}_\sigma$.

III. SPECTRAL PROPERTIES OF KMR MODEL IN SC

A. Energy spectra

In Fig. 2, we show the energy spectra and density of states (DOS) of the model Hamiltonian \mathcal{H}_{KMR} , for the

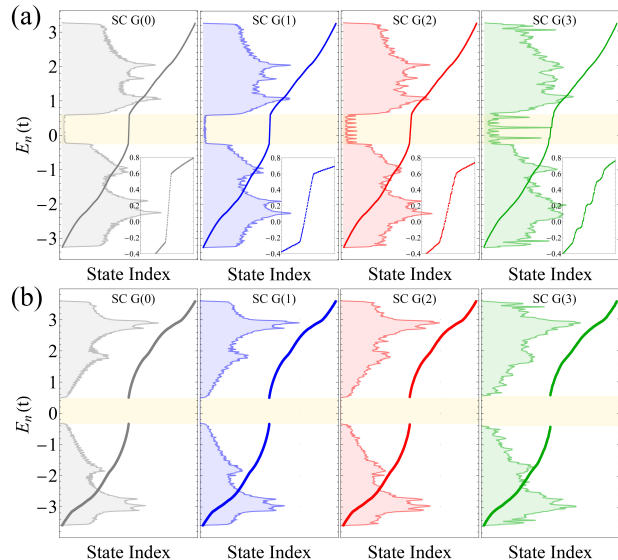


FIG. 2. Energy spectra and DOS for $\lambda_{\text{KM}} = 0.25t$ and $\lambda_{\text{R}} = \sqrt{3}\lambda_{\text{KM}} \approx 0.43t$ at (a) QSHI ($V_{\text{ab}} = 0$) and (b) trivial phase ($V_{\text{ab}} = 7\sqrt{3}t/8 \approx 1.51t$). Results for G(0-3) appear in gray, blue, red, and green. The light-yellow region marks the bulk band gap (Δ^{E}) of the homogeneous Kane-Mele-Rashba model. Insets in (a) zoom into this region, highlighting the topological states inside the gap with the staircase profile.

four generations of the SC presented in Fig. 1. Unless explicitly stated otherwise, we consider the model's parameters $\lambda_{\text{KM}} = 0.25t$, $\lambda_{\text{R}} = \sqrt{3}\lambda_{\text{KM}} \approx 0.43t$ with

$V_{ab} = 0$ for the QSHI phase and $V_{ab} = 7\sqrt{3}t/8$ for the topologically trivial phase. These sets of parameters are chosen conveniently and marked as the two red targets in the schematic diagram at the lower left part of Fig. 1. Figs. 2(a) and (b) show the results with model parameters adjusted to match the QSHI phase and the topologically trivial phase, respectively. The OBC used leads to in-gap topological states when the model's parameters are adjusted to reach a QSHI phase [see Fig. 2(a)].

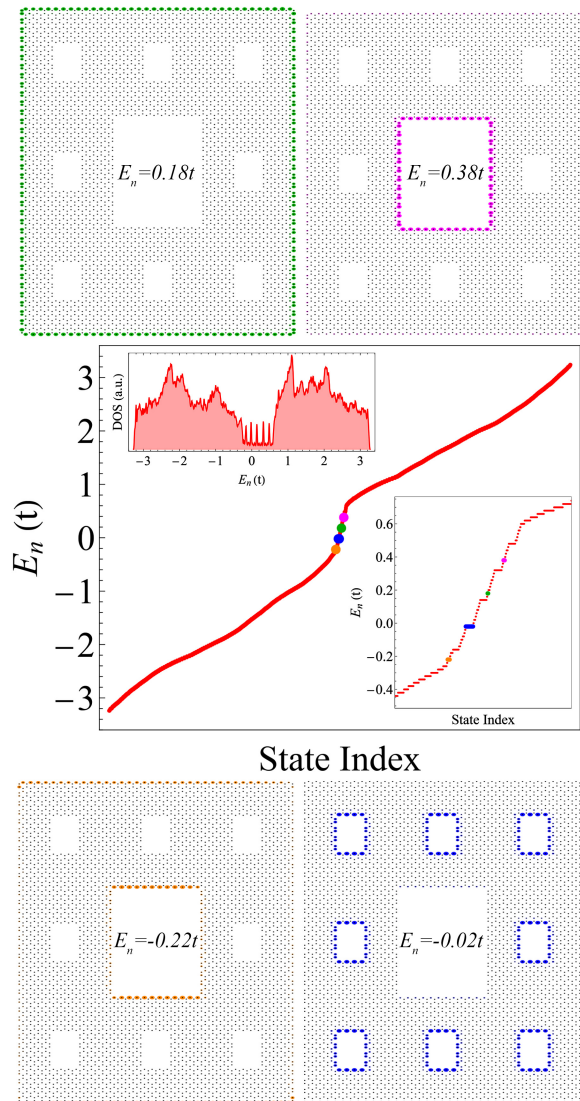


FIG. 3. Energy spectra in function of the state index with length of $\dim(\mathcal{H}_{\text{KMR}})$. The insets, superior and inferior, for the DOS and zooming the staircase states, respectively. Panels on top and bottom of the energy spectra show the squared modulus of the electronic wave function for in-gap topological states at different energies: $E_n = -0.22t$, $-0.02t$, $0.18t$, and $0.38t$, in orange, blue, green and magenta, respectively. The considered SC $G(2)$ is in the QSHI phase with $\lambda_{\text{KM}} = 0.25t$, $\lambda_{\text{R}} = \sqrt{3}\lambda_{\text{KM}} \approx 0.43t$ and $V_{ab} = 0$.

The in-gap states are absent in the topologically trivial

situations [Fig. 2(b)]. In both the QSHI and trivial phases, the bulk states are not significantly affected by the fractality of the system. The general profile of these energy levels remains nearly unchanged as the fractal generation increases. The respective DOS takes on a noisy appearance with the introduction of fractality. This behavior of bulk energy levels and DOS is consistent with previous studies on SC on a honeycomb mesh, as reported in Refs. [12, 38, 40]. However, the fractal structure drastically alters the in-gap topological states in the QSHI phase, producing a staircase-like profile in this energy spectrum region as the fractal generation increases. This staircase profile shown in the insets of Fig. 1(a), translates into sharp peaks in the DOS.

In Fig. 3, we show the energy spectra of a SC $G(2)$ in the QSHI phase, considering a lower mesh with $N = 4256$ sites to avoid computational expenses. It is important to mention that the result captures the physical aspects of wave functions in SCs with denser meshes used in the other numerical results of the present work [Fig. 1]. In fact, in previous work, we showed that the charge distribution converges to a final pattern for a sufficient number of sites [6]. We also show the wave-function square modulus of topological states at different in-gap energy levels. When an energy level is degenerated due to the staircase profile, we plot the sum of the square moduli of the wave functions in the degenerate subspace and apply a normalization factor. We highlight two key aspects of the distributions shown in Fig. 3: (i) The in-gap states closer to the system's neutrality point are localized at the outer edge of SC $G(2)$, as expected from the QSHI picture. The other in-gap states at different energy levels are localized at internal edges formed by the voids introduced in the fractal Sierpinski system. (ii) The distributions obey the C_2 symmetry of a SC in the underlying honeycomb mesh, as discussed in Sec. II A. For the other states outside the in-gap solutions, the LDOS map is distributed regularly over the SC sites, as expected for bulk states.

B. Valence projected spin-spectra

As discussed in Sec. II B, the topological indexation by the LSCM is only possible in the presence of a finite valence-projected spin gap Δ^{s_z} . As previously reported [35], the existence of this gap is not guaranteed by any physical constraint and is associated with the specific details of the model under study. The requirement of a finite Δ^{s_z} can be seen as a limitation of the approach. Nevertheless, when the valence-projected spin spectra present a finite gap, indexing via the spin Chern number is possible and conveys the same physical information as the \mathbb{Z}_2 invariant in time-reversal symmetric systems [56, 57].

In Fig. 4, we present the valence-projected spin spectra $\xi_v^{s_z}$ as a function of the normalized state indexes, for the Kane-Mele-Rashba model in both the QSHI and trivial

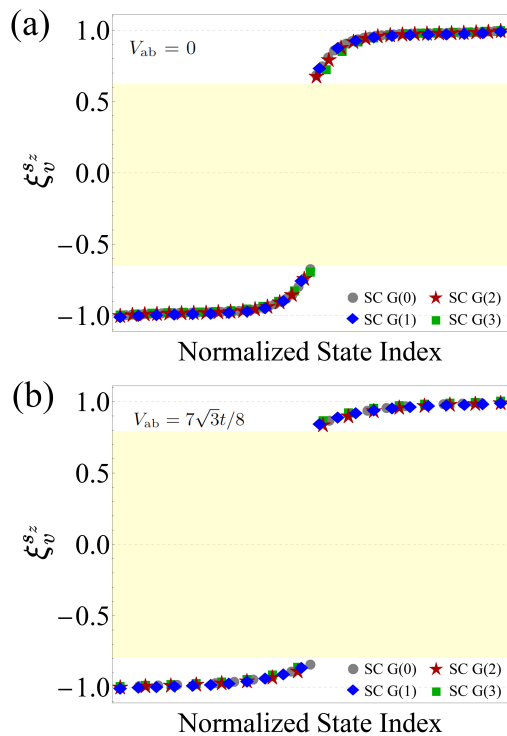


FIG. 4. Valence projected spin spectra of the Kane-Mele-Rashba model with $\lambda_{\text{KM}} = 0.25t$, $\lambda_{\text{R}} = \sqrt{3}\lambda_{\text{KM}} \approx 0.43t$ and (a) $V_{\text{ab}} = 0$ [QSHI phase] and (b) $V_{\text{ab}} = 7\sqrt{3}t/8 \approx 1.51t$ [trivial phase]. The spectra for different fractal generations is given as a function of the ‘normalized state index’ = ‘state index’/ N_{occ} .

phases across different fractal generations. The numbers of occupied states at half-filling for the different fractal generations represented in Fig. 1 are: $N_{\text{occ}} = 11988$ for SC G(0), $N_{\text{occ}} = 10512$ for SC G(1), $N_{\text{occ}} = 9456$ for SC G(2), and $N_{\text{occ}} = 8688$ for SC G(3). The light-yellow rectangle represents the gap Δ^{s_z} . One notices that increasing the fractal generation barely alters the valence-projected spin gap Δ^{s_z} in both the QSHI and trivial phases. This is a remarkable result in this work and means that the LSCM method can be applied to the Kane-Mele-Rashba model at high-fractal generations of the SC. In the next section, we use this approach to study the local topology of the system.

IV. LOCAL TOPOLOGY IN SC VIA LSCM

The robustness of the valence-projected spin gap Δ^{s_z} with increasing fractal generation, as presented in Fig. 4, suggests the LSCM method can be applied to locally index the topology of the wave function. This approach was originally introduced in Refs. [33, 54, 55] and combines those of Prodan [35] and Bianco-Resta [34]. It has been shown to accurately capture the topological phase diagram of the Kane-Mele-Rashba model [33] and

its generalizations [36].

We show in Fig. 5 the results for the LSCM in the sites along the lines depicted in Fig. 1, marked with different colors, and for the four fractal generations considered. The Hamiltonian parameters in Fig. 5(a)-(d) were chosen to match the QSHI phase.

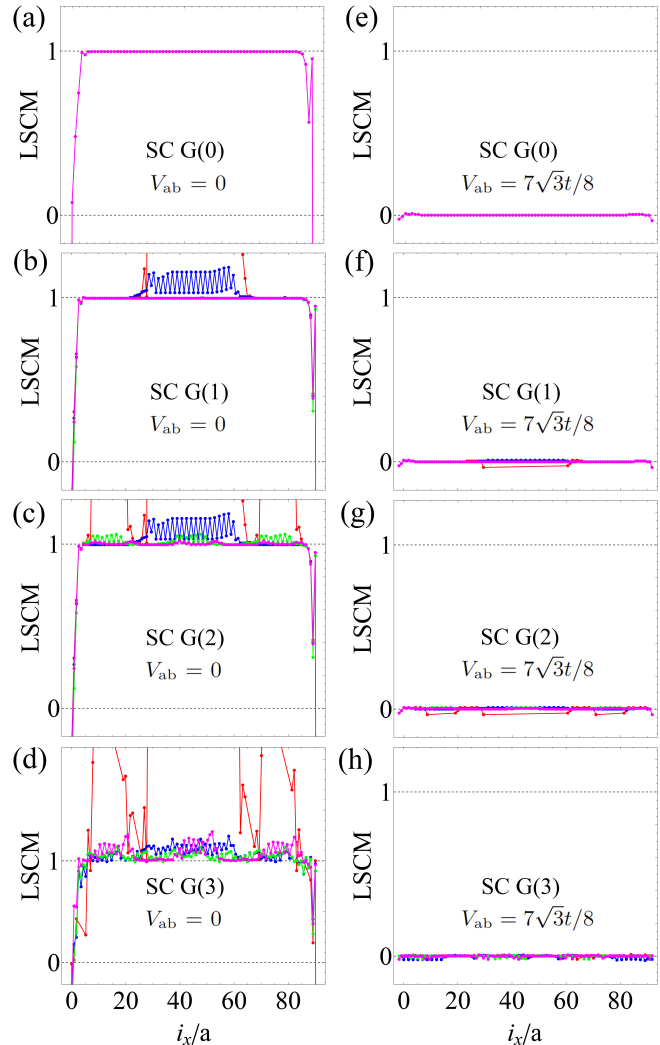


FIG. 5. LSCM for SC of G(0-3) (a-d) $V_{\text{ab}} = 0$ [QSHI phase] and (e-h) $V_{\text{ab}} = 7\sqrt{3}t/8$ [trivial phase]. We set $\lambda_{\text{KM}} = 0.25t$, $\lambda_{\text{R}} = \sqrt{3}\lambda_{\text{KM}}$. The colors of the curves follow the color convention of the arrows depicted in Fig. 1: red, blue, magenta, and green curves corresponding to arrows (I), (II), (III), and (IV), respectively. Here, a is the nearest neighbor distance in the honeycomb arrangement.

For the SC G(0) in the QSHI phase [Fig. 5(a)] the LSCM along lines (I), (II), (III) and (IV) is quantized for sites in the bulk of the system \mathbf{i}_{bulk} , $\mathbf{c}_s(\mathbf{i}_{\text{bulk}}) = 1$. Near the edges sites $\mathbf{i}_{\text{edges}}$, the LSCM exhibit well-known anomalies characteristic of local markers [34]. Here, we performed our calculations using OBC, but this behavior also occurs in systems with periodic boundary conditions [36, 58]. Proposals to solve these anomalies involve

different enumeration in position operators [22, 59]. In the case of SC G(1) in the QSHI phase [Fig. 5(b)], the central void disrupts the quantization of LSCM along lines (I) and (II) in the region $30 \lesssim i_x/a \lesssim 60$. However, the quantization of the marker is preserved along these lines for sites in the regions $5 \lesssim i_x/a \lesssim 30$ and $60 \lesssim i_x/a \lesssim 85$, corresponding to internal sites.

Lines (III) and (IV) are far from the central void in SC G(1) and are not influenced by its internal edge, thus maintaining the quantization of LSCM in the entire region $5 \lesssim i_x/a \lesssim 85$ enough distant from external edges. As the fractal generation increases by introducing more voids in the system, we observe from Fig. 5(c) and (d) that regions with anomalies proliferate due to the increasing influence of internal edge regions in sites crossed by lines (I)-(IV). For sites sufficiently far from edges of the system, the LSCM remains quantized. An interesting feature of Figs. 5(b)-(d) is that the anomalies in the internal edges caused by the voids have the opposite sign compared to those in the external edges.

In Fig. 5(e)-(h) we report an analogous result but with the Hamiltonian parameter adjusted to match the topologically trivial phase. In this situation, the LSCM takes a value consistent with zero throughout the entire system for different fractal generations. The internal edges introduced by the voids in each fractal generation, merely cause tiny oscillations (of the order $\lesssim 10^{-2}$) of the LSCM. This shows that the LSCM also correctly indexes the topologically trivial phase, which is ensured by the existence of a finite spin gap, shown in Fig. 4(b).

To complement our analysis, we present in Fig. 6 the site-resolved LSCM in the SC G(3) fractal as a color map across the system for both the QSHI [Fig. 6(a)] and topologically trivial [Fig. 6(b)] phases. One can observe that, despite the presence of many voids in the SC G(3), the LSCM marker remains quantized in a significant portion of the fractal system. For sites located one hexagon away from any edge (internal or external), the quantization of the LSCM $\mathcal{C}_s \approx 1$ is achieved in the QSHI phase [Fig. 6(a)]. In the trivial phase, one obtains $\mathcal{C}_s \approx 0$ in almost the entire system [Fig. 6(b)]. Fig. 6 shows the ability of this marker to accurately capture the local topological indexation of the system for both phases of the Kane-Mele-Rashba phase diagram in SC fractal geometry. As one approaches the mathematical limit of the SC fractal by increasing the generation further, anomalies caused by internal edges from numerous voids become dominant, compromising the quantization of the marker in QSHI. We emphasize here that both negative and positive divergences, marked as black and gray sites in Fig. 6(a), respectively, are present in the LSCM spatialmap. However, the \mathcal{C}_s legend color bar is cut at the relevant range which is between 0 and 1 values.

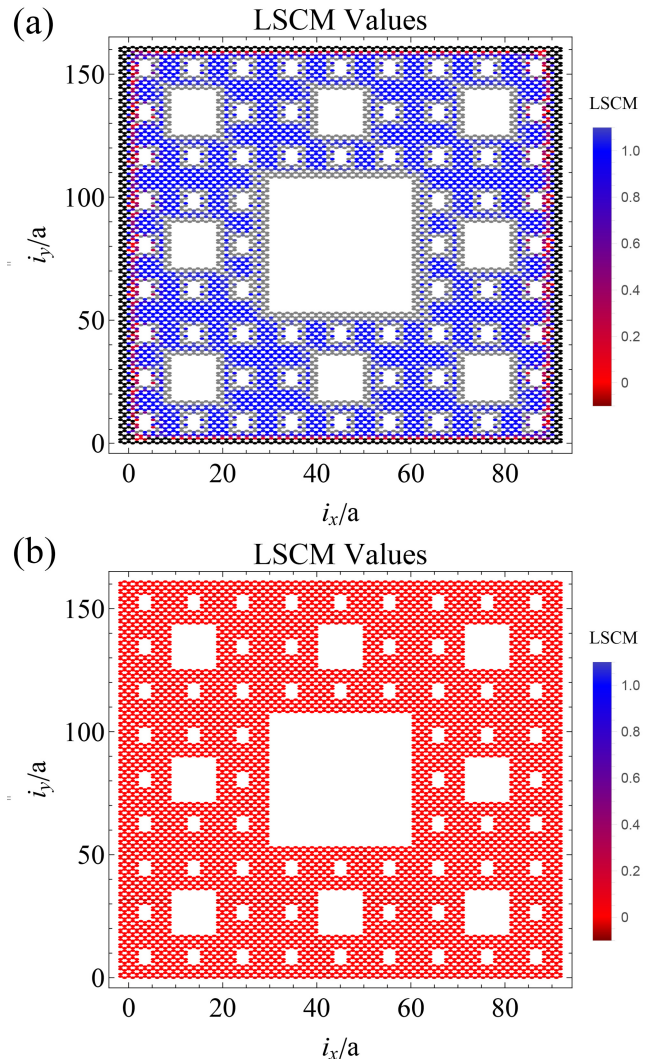


FIG. 6. Site-resolved LSCM for SC G(3). We set $\lambda_{\text{KM}} = 0.25t$, $\lambda_{\text{R}} = \sqrt{3}\lambda_{\text{KM}}$ and sublattice potential (a) $V_{ab} = 0$ [QSHI phase] and (b) $V_{ab} = 7\sqrt{3}t/8$ [trivial phase].

V. FINAL REMARKS

Comparison to other topological indexes: Different methods for indexing the topology of quantum fractals have been employed in literature. Examples include methods based on the Bott index [9, 60, 61] and the real-space version of the global Chern number proposed by Kitaev [7, 11, 62–64]. As discussed in Ref. [7], methods based on the Bott index require the artificial introduction of periodic boundary conditions, which may be inconvenient for fractal structures that typically occur in systems with open boundary conditions. On the other hand, the Chern number method in real space proposed by Kitaev [65] depends on a rather ambiguous and complicated choice of partitioning the system into distinct regions, although it captures the topological aspects of fractals at high generations, when only a small

bulk region is available.

Site-spacing limit: The study of quantum fractals in lattice models is inherently constrained by the number of sites used in their construction [14]. Starting with a larger number of sites in a SC $G(0)$ structure allows for the introduction of more voids in the system in a self-similar manner before reaching the site-spacing limit. This results in larger fractal generations with a more significant bulk region. As discussed above, a bulk region with at least one hexagon of distance from the internal/external edge of the system is necessary for the marker to present a quantized value in the QSHI phase, for the set of parameters used in previous sections. These limitations mean that computational power is an important issue in the type of study presented in this work.

VI. CONCLUSIONS

In this work, we present a detailed study of the spectral properties and local topology of the Kane-Mele-Rashba model on a SC fractal constructed over an underlying honeycomb mesh. In the quantum spin Hall insulator phase, the in-gap topological states in the model's energy spectrum exhibit a staircase profile as the fractal generation of the SC increases. This staircase

profile in energy spectra translates into the appearance of sharp peaks in the density of states in the in-gap energy region. We also show that the valence-projected spin spectrum exhibits a gap Δ^{sz} in both the quantum spin Hall insulator and the trivial phases, which remains robust against an increase in fractal generation. This enables the definition of a local spin Chern marker that captures the spatially resolved topology of the quantum spin Hall insulating phase. We numerically computed the local spin Chern marker in a flake with a large number of sites, showing that this topological marker captures the expected behavior up to the third fractal generation of the Sierpinski carpet. Our work may be useful for the comprehension of topological quantum fractals and expands the scope of local spin Chern marker methods to applications in complex fractal geometry.

ACKNOWLEDGMENTS

The authors would like to thank the INCT de Nanomateriais de Carbono for providing support on the computational infrastructure. LLL thanks the CNPq scholarship. SAS-J gratefully acknowledges financial support from the Brazilian Agency CNPq. AL thanks FAPERJ under grant E-26/200.569/2023. The authors thank Rodrigo Arouca for fruitful discussions.

-
- [1] J. Shang, Y. Wang, M. Chen, J. Dai, X. Zhou, J. Kuttner, G. Hilt, X. Shao, J. M. Gottfried, and K. Wu, *Nature Chemistry* **7**, 389 (2015).
- [2] S. N. Kempkes, M. R. Slot, S. E. Freney, S. J. M. Zevenhuizen, D. Vanmaekelbergh, I. Swart, and C. M. Smith, *Nature Physics* **15**, 127 (2019).
- [3] J. Li, Q. Mo, J.-H. Jiang, and Z. Yang, *Science Bulletin* **67**, 2040 (2022).
- [4] Z. Yang, E. Lustig, Y. Lumer, and M. Segev, *Light: Science & Applications* **9**, 128 (2020).
- [5] L. L. Lage and A. Latgé, *Phys. Chem. Chem. Phys.* **24**, 19576 (2022).
- [6] L. L. Lage, N. C. Rappe, and A. Latgé, *Journal of Physics: Condensed Matter* **37**, 025303 (2024).
- [7] Z. F. Osseweijer, L. Eek, A. Moustaj, M. Fremling, and C. Morais Smith, "Haldane model on the sierpiński gasket," (2024).
- [8] A. A. Iliasov, M. I. Katsnelson, and S. Yuan, *Phys. Rev. B* **101**, 045413 (2020).
- [9] J. Li, Y. Sun, Q. Mo, Z. Ruan, and Z. Yang, *Phys. Rev. Res.* **5**, 023189 (2023).
- [10] E. van Veen, A. Tomadin, M. Polini, M. I. Katsnelson, and S. Yuan, *Phys. Rev. B* **96**, 235438 (2017).
- [11] M. Brzezińska, A. M. Cook, and T. Neupert, *Phys. Rev. B* **98**, 205116 (2018).
- [12] E. van Veen, S. Yuan, M. I. Katsnelson, M. Polini, and A. Tomadin, *Phys. Rev. B* **93**, 115428 (2016).
- [13] M. Toloza Sandoval, A. Araújo, F. Crasto de Lima, and A. Fazzio, *Physica E: Low-dimensional Systems and Nanostructures* **165**, 116097 (2025).
- [14] S. Fischer, M. van Hooft, T. van der Meijden, C. M. Smith, L. Fritz, and M. Fremling, *Phys. Rev. Res.* **3**, 043103 (2021).
- [15] M. Z. Hasan and C. L. Kane, *Rev. Mod. Phys.* **82**, 3045 (2010).
- [16] F. D. M. Haldane, *Phys. Rev. Lett.* **61**, 2015 (1988).
- [17] C. L. Kane and E. J. Mele, *Phys. Rev. Lett.* **95**, 226801 (2005).
- [18] C. L. Kane and E. J. Mele, *Phys. Rev. Lett.* **95**, 146802 (2005).
- [19] A. Altland and M. R. Zirnbauer, *Phys. Rev. B* **55**, 1142 (1997).
- [20] S. Ryu, A. P. Schnyder, A. Furusaki, and A. W. W. Ludwig, *New Journal of Physics* **12**, 065010 (2010).
- [21] B. D. Assunção, G. J. Ferreira, and C. H. Lewenkopf, *Phys. Rev. B* **109**, L201102 (2024).
- [22] L. A. Oliveira and W. Chen, *Phys. Rev. B* **109**, 094202 (2024).
- [23] S.-W. Kim, S. Jeon, M. J. Park, and Y. Kim, *npj Computational Materials* **9** (2023), 10.1038/s41524-023-01105-5.
- [24] E. Drigo and R. Resta, *Phys. Rev. B* **101**, 165120 (2020).
- [25] P. B. Melo, S. a. A. S. Júnior, W. Chen, R. Mondaini, and T. Paiva, *Phys. Rev. B* **108**, 195151 (2023).
- [26] I. Gilardoni, F. Becca, A. Marrazzo, and A. Parola, *Phys. Rev. B* **106**, L161106 (2022).
- [27] A. A. Markov and A. N. Rubtsov, *Phys. Rev. B* **104**, L081105 (2021).
- [28] T. G. Pedersen, *Phys. Rev. B* **101**, 235427 (2020).

- [29] E. Domany, S. Alexander, D. Bensimon, and L. P. Kadanoff, *Phys. Rev. B* **28**, 3110 (1983).
- [30] R. Rammal and G. Toulouse, *Phys. Rev. Lett.* **49**, 1194 (1982).
- [31] L. Eek, Z. F. Osseweijer, and C. M. Smith, “Fractality-induced topology,” (2024), arXiv:2411.12341 [cond-mat.mes-hall].
- [32] R. Canyellas, C. Liu, R. Arouca, L. Eek, G. Wang, Y. Yin, D. Guan, Y. Li, S. Wang, H. Zheng, C. Liu, J. Jia, and C. Morais Smith, *Nature Physics* **20**, 1421 (2024).
- [33] N. Baù and A. Marrazzo, *Phys. Rev. B* **110**, 054203 (2024).
- [34] R. Bianco and R. Resta, *Phys. Rev. B* **84**, 241106 (2011).
- [35] E. Prodan, *Phys. Rev. B* **80**, 125327 (2009).
- [36] S. d. A. Sousa-Júnior, M. V. d. S. Ferraz, J. P. de Lima, and T. P. Cysne, *Phys. Rev. B* **111**, 035411 (2025).
- [37] X. Yang, W. Zhou, Q. Yao, P. Lv, Y. Wang, and S. Yuan, *Phys. Rev. B* **105**, 205433 (2022).
- [38] G. Bouzerar and D. Mayou, *Phys. Rev. Res.* **2**, 033063 (2020).
- [39] D. Han, H. Fan, X. Wang, and L. Cheng, *Materials Research Express* **7**, 035020 (2020).
- [40] X. Yang, W. Zhou, Q. Yao, Y. Li, Y. Wang, and S. Yuan, *Phys. Rev. B* **109**, 235429 (2024).
- [41] T. P. Cysne, A. Ferreira, and T. G. Rappoport, *Phys. Rev. B* **98**, 045407 (2018).
- [42] K.-H. Jin and S.-H. Jhi, *Phys. Rev. B* **87**, 075442 (2013).
- [43] K. Song, D. Soriano, A. W. Cummings, R. Robles, P. Ordejón, and S. Roche, *Nano Letters* **18**, 2033 (2018), PMID: 29481087, <https://doi.org/10.1021/acs.nanolett.7b05482>.
- [44] M. Gmitra, D. Kochan, P. Högl, and J. Fabian, *Phys. Rev. B* **93**, 155104 (2016).
- [45] W. Han, R. K. Kawakami, M. Gmitra, and J. Fabian, *Nature Nanotechnology* **9**, 794–807 (2014).
- [46] A. Avsar, H. Ochoa, F. Guinea, B. Özyilmaz, B. J. van Wees, and I. J. Vera-Marun, *Rev. Mod. Phys.* **92**, 021003 (2020).
- [47] K. Zollner and J. Fabian, *2D Materials* **12**, 013004 (2024).
- [48] M. Ezawa, *Phys. Rev. Lett.* **109**, 055502 (2012).
- [49] M. Ezawa, *Journal of the Physical Society of Japan* **84**, 121003 (2015).
- [50] C.-C. Liu, H. Jiang, and Y. Yao, *Phys. Rev. B* **84**, 195430 (2011).
- [51] G. Li, W. Hanke, E. M. Hankiewicz, F. Reis, J. Schäfer, R. Claessen, C. Wu, and R. Thomale, *Phys. Rev. B* **98**, 165146 (2018).
- [52] F. Reis, G. Li, L. Dudy, M. Bauernfeind, S. Glass, W. Hanke, R. Thomale, J. Schäfer, and R. Claessen, *Science* **357**, 287–290 (2017).
- [53] Y. A. Bychkov and E. I. Rashba, *Journal of Physics C: Solid State Physics* **17**, 6039 (1984).
- [54] W. Chen, *Journal of Physics: Condensed Matter* **35**, 165601 (2023).
- [55] K.-S. Lin, G. Palumbo, Z. Guo, Y. Hwang, J. Blackburn, D. P. Shoemaker, F. Mahmood, Z. Wang, G. A. Fiete, B. J. Wieder, and B. Bradlyn, *Nature Communications* **15** (2024), 10.1038/s41467-024-44762-w.
- [56] A. A. Soluyanov and D. Vanderbilt, *Phys. Rev. B* **85**, 115415 (2012).
- [57] T. Fukui and Y. Hatsugai, *Phys. Rev. B* **75**, 121403 (2007).
- [58] W. Chen, *Phys. Rev. B* **107**, 045111 (2023).
- [59] A. A. Aligia, *Phys. Rev. B* **107**, 075153 (2023).
- [60] P. Lai, H. Liu, B. Xie, W. Deng, H. Wang, H. Cheng, Z. Liu, and S. Chen, *Phys. Rev. B* **109**, L140104 (2024).
- [61] S. Manna, S. K. Das, and B. Roy, *Phys. Rev. B* **109**, 174512 (2024).
- [62] S. Pai and A. Prem, *Phys. Rev. B* **100**, 155135 (2019).
- [63] Y.-k. Chen, Q.-h. Liu, B. Zou, and Y. Zhang, *Phys. Rev. B* **107**, 054109 (2023).
- [64] S. Sarangi and A. E. B. Nielsen, *Phys. Rev. B* **104**, 045147 (2021).
- [65] A. Kitaev, *Annals of Physics* **321**, 2 (2006), january Special Issue.